Debonding of short fibres among particulates in a metal matrix composite

Viggo Tvergaard [*]

*Department of Mechanical Engineering, Solid Mechanics, Technical University of Denmark,
Building 404, DK-2800 Kgs. Lyngby, Denmark*

Abstract

A numerical analysis is carried out for the development of damage by fibre–matrix debonding in aluminium reinforced by aligned, short SiC fibres. A unit cell-model that has earlier been applied to study materials with arrays of transversely staggered fibres is here extended to contain a number of differently shaped fibres or particulates in each unit cell, thus representing debonding of a relatively long discontinuous fibre among particulates that do not debond. Interfacial failure is modelled in terms of a cohesive zone model that accounts for decohesion by normal separation as well as by tangential separation. It is found that the evolution of failure can depend rather strongly on the distribution of particulates around a fibre subject to debonding.
© 2003 Elsevier Ltd. All rights reserved.

1. Introduction

Metals reinforced by short brittle fibres have increased stiffness and tensile strength, but the reinforcement also leads to poor ductility and low fracture toughness (Divecha et al., 1981; McDanels, 1985; Zok et al., 1988). Debonding of the matrix–fibre interface or fibre breakage can result in early void formation, and also ductile matrix failure can be promoted by the stress and strain concentrations occurring around sharp fibre edges (Needleman et al., 1993). To improve the overall material behaviour, a parametric understanding of the effect of different material parameters is important, as can be obtained by numerical cell-model analyses. Such analyses are an important tool, as they allow for an accurate representation of the fibre shape, the volume fraction, the strength of the interface and the fibres, and the matrix yield stress and strain hardening, thus leading to realistic stress and strain fields around the fibres. The different failure mechanisms have been studied in a number of cell-model analyses (Nutt and Needleman, 1987; Tvergaard, 1993, 1998; Finot et al., 1994). Studies of fracture in metals reinforced by long fibres, follow somewhat different procedures, as e.g. discussed by Dvorak et al. (1992).

[*] Tel.: +45-4525-4273; fax: +45-4593-1475.
E-mail address: viggo@mek.dtu.dk (V. Tvergaard).

The present investigation is focussed on failure by matrix–fibre debonding, using a cohesive zone model that describes decohesion by any mixture of normal separation and tangential separation (Tvergaard, 1990b, 1991). Effects of fibre clustering are important, but still most cell-model analyses have considered a characteristic material volume containing only a single fibre, which does not allow for clustering. In a plane strain model of a discontinuously reinforced metal it is rather easy to include many fibres with different shapes and spacings in a unit cell, thus representing some degree of clustering, but the plane strain models have the disadvantage that fibre geometries are not realistically represented (e.g. see Needleman et al., 1993). On the other hand, axisymmetric cell-models allow for rather realistic fibre geometries, without enforcing the complications of a full three dimensional numerical analysis. Therefore, an axisymmetric cell-model will be used here, which includes other short fibres than those undergoing debonding along the matrix–fibre interface. By also using a special cell-model that represents transversely staggered arrays of fibres (Tvergaard, 1990a), it is possible here to study the effect of fibres that fail by debonding while surrounded by fibres that do not fail. The results will be compared with predictions for simple periodic arrays of fibres, as in Tvergaard (1990b), where all fibres fail simultaneously.

2. Problem formulation

The axisymmetric unit cell-model to be used here is that also used by Tvergaard (1990b) for the study of debonding in a periodic array of aligned fibres that can be represented by taking only one fibre inside each unit cell (see Fig. 1). For this case a cross-section perpendicular to the fibres (Fig. 1(b)) shows a square array of fibres with spacing $2a_c$, and the initial radius $r_c = (2/\sqrt{\pi})a_c$ of the axisymmetric model problem is chosen such that the fibre volume fraction of the cell is equal to that of the material illustrated in Fig. 1. With the initial cell length ℓ_c, and the fibre geometry specified by the initial half length ℓ_f and radius r_f, the fibre volume fraction f in the case of one fibre is $f = (r_f^2 \ell_f)/(r_c^2 \ell_c)$. Then the initial aspect ratios of the fibre and cell, respectively, are specified by $\alpha_f = \ell_f/r_f$, $\alpha_c = \ell_c/r_c$. The periodic fibre array shown in Fig. 1 corresponds to one of the materials to be analysed here (i.e. material A in Fig. 3).

The boundary conditions applied for this cell-model with transversely staggered fibres are specified by the following considerations. On the curved side of the circular cylindrical cell, equilibrium and compatibility with the neighbouring cells has to be represented in an approximate manner. A neighbouring cell is identical to that analysed, but is rotated 180° so that it points in the opposite direction (see Fig. 1(a)).
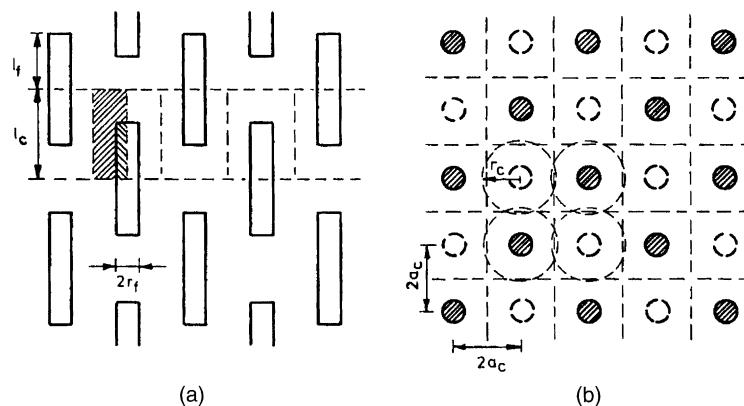

Fig. 1. Transversely staggered periodic array of aligned fibres, in a case where the unit cell contains only one fibre (as in material A, Fig. 3), (a) cross-section along fibres and (b) cross-section normal to fibres.

Compatibility and equilibrium in the axial direction are directly specified in terms of the axial edge displacements and nominal tractions. In the radial direction compatibility is represented by the requirement that the total cross-sectional area (consisting of an equal number of cross-sections of the two types of neighbouring cells considered) is independent of the axial coordinate (see Tvergaard, 1990a,b).

When U_1 denotes the increase of the length of the cell, and U_2 is the radius increase at the centre of the cell (at $x^1 = \ell_c/2$), the average logarithmic strains in the axial and transverse directions are $\epsilon_1 = ln(1 + U_1/\ell_c)$ and $\epsilon_2 = ln(1 + U_2/r_c)$, respectively. The average nominal stresses Σ_{ij} are computed as the appropriate area averages of the microscopic nominal stress components on the surface (considering both the cell analysed and one of the neighbouring cells of opposite kind). The axial and transverse Cartesian stress components are Σ_{11} and $\Sigma_{22} = \Sigma_{33}$, respectively, for the axisymmetric problem, and all shear components vanish. Using the average strains ϵ_1 and ϵ_2, the average true stresses σ_1 and σ_2 are calculated from the nominal stress values.

The same set of boundary conditions also applies to a unit cell with more than one fibre along the axis, as long as the neighbouring cell is identical to that analysed, but is rotated 180° so that it points in the opposite direction. Such two neighbouring cells are shown in Fig. 2, with the dimensions and the positions of the additional two fibres specified by ℓ_1, r_1, a_1 and ℓ_2, r_2, a_2, respectively. The analyses here will consider cells as that shown in Fig. 2 and compare with predictions for the cell in Fig. 1, for equal values of the total fibre volume fractions, which is now given by

$$f = \left(r_f^2\ell_f + r_1^2\ell_1 + r_2^2\ell_2\right)/r_c^2\ell_c \tag{2.1}$$

As in Tvergaard (1990b) the matrix material deformations are taken to be described by J_2 flow theory with isotropic hardening. A convected coordinate, Lagrangian formulation of the field equations is used, in which g_{ij} and G_{ij} are metric tensors in the reference configuration and the current configuration, respectively, with determinants g and G, and $\eta_{ij} = 1/2(G_{ij} - g_{ij})$ is the Lagrangian strain tensor. The contravariant components τ^{ij} of the Kirchhoff stress tensor on the current base vectors are related to the
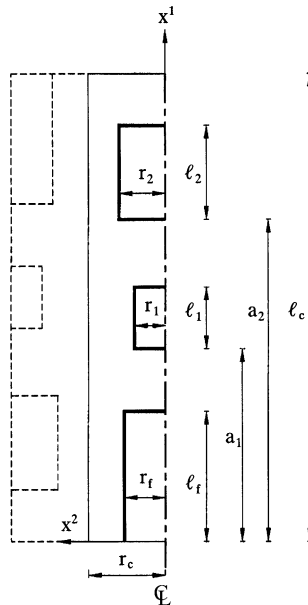

Fig. 2. The axisymmetric unit cell containing three different short fibres. The neighbouring cell, rotated 180°, is indicated by dashed lines.
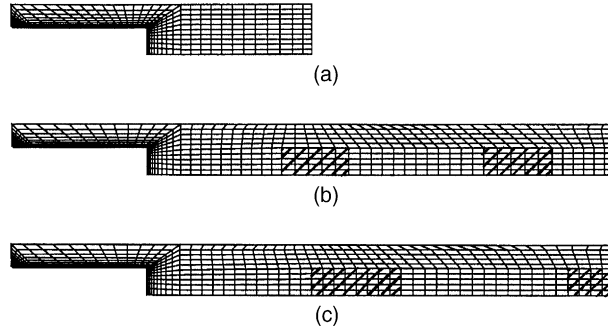
Fig. 3. Initial meshes used: (a) material A; (b) material B and (c) material C.

components of the Cauchy stress tensor σ^{ij} by $\tau^{ij} = \sqrt{G/g}\sigma^{ij}$. The finite strain generalization of J_2 flow theory, in which the incremental stress–strain relationship is of the form $\dot{\tau}^{ij} = L^{ijk\ell}\dot{\eta}_{k\ell}$, has the tensor of instantaneous moduli given by

$$L^{ijk\ell} = \frac{E}{1+v}\left\{ \frac{1}{2}\left(G^{ik}G^{j\ell} + G^{i\ell}G^{jk}\right) + \frac{v}{1-2v}G^{ij}G^{k\ell} - \beta\frac{3/2(E/E_t - 1)}{E/E_t - (1-2v)/3}\frac{s^{ij}s^{k\ell}}{\sigma_e^2} \right\}$$
$$- \frac{1}{2}\left(G^{ik}\tau^{j\ell} + G^{jk}\tau^{i\ell} + G^{i\ell}\tau^{jk} + G^{j\ell}\tau^{ik}\right) \tag{2.2}$$

Here, $s^{ij} = \tau^{ij} - G^{ij}\tau_k^k/3$ is the stress deviator, the effective Mises stress is $\sigma_e = (3s_{ij}s^{ij}/2)^{1/2}$, the value of β is 1 or 0 for plastic yielding or elastic unloading, respectively, E is Young's modulus, v is Poisson's ratio, and E_t is the slope of the true stress vs natural strain curve at the stress level σ_e. The uniaxial stress–strain behaviour is represented by

$$\epsilon = \begin{cases} \dfrac{\sigma}{E} & \text{for } \sigma \leqslant \sigma_y \\ \dfrac{\sigma_y}{E}\left(\dfrac{\sigma}{\sigma_y}\right)^n & \text{for } \sigma > \sigma_y \end{cases} \tag{2.3}$$

where σ_y is the uniaxial yield stress, and n is the strain hardening exponent.

The debonding behaviour is specified in terms of a cohesive zone model proposed by Tvergaard (1990b) as an extension of the model by Needleman (1987) to also account for tangential separation. A set of interface constitutive relations give the dependence of the normal and tangential tractions T_n and T_t on the corresponding components u_n and u_t of the displacement difference across the interface.

A nondimensional parameter λ is defined as

$$\lambda = \sqrt{\left(\frac{u_n}{\delta_n}\right)^2 + \left(\frac{u_t}{\delta_t}\right)^2} \tag{2.4}$$

and a function $F(\lambda)$ is chosen as

$$F(\lambda) = \frac{27}{4}\sigma_{\max}(1 - 2\lambda + \lambda^2), \quad \text{for } 0 \leqslant \lambda \leqslant 1 \tag{2.5}$$

Then, as long as λ is monotonically increasing, the interface tractions are taken to be given by the expressions

$$T_n = \frac{u_n}{\delta_n}F(\lambda), \quad T_t = \alpha\frac{u_t}{\delta_t}F(\lambda) \tag{2.6}$$

In purely normal separation ($u_t \equiv 0$) the maximum traction is σ_{max}, total separation occurs at $u_n = \delta_n$, and the work of separation per unit interface area is $9\sigma_{max}\delta_n/16$. In purely tangential separation ($u_n \equiv 0$) the maximum traction is $\alpha\sigma_{max}$, total separation occurs at $u_t = \delta_t$, and the work of separation per unit interface area is $9\alpha\sigma_{max}\delta_t/16$. The values of the four parameters δ_n, δ_t, σ_{max} and α have to be chosen such that the maximum traction and work of separation in different situations are well approximated. The incremental constitutive relations for the interface, needed in numerical solutions, are directly obtained from (2.6). These expressions apply for $\dot{\lambda} \geqslant 0$ and $\lambda = \lambda_{max} < 1$, while for decreasing λ a type of elastic unloading is used to represent the partly damaged interface (see Tvergaard, 1990b). Furthermore, under normal compression elastic springs with high stiffness are used to approximately represent contact, and also friction between fibre and matrix after the occurrence of debonding is readily incorporated in the formulation.

The debonding model (2.4)–(2.6) is used for the matrix–fibre interface along the fibre with length ℓ_f and radius r_f in Fig. 2, and for convenience this fibre is modelled as rigid, while the other two fibres are modelled as elastic. It has been found for perfectly bonded SiC whisker-reinforced aluminium (Tvergaard, 1990a) that predictions for elastic or rigid fibres differ rather little when plastic yielding has occurred, since the fibre elastic modulus is much higher than that of aluminium ($E_f \simeq 5.7E_{Al}$). Therefore, the convenient choice of modelling one fibre as rigid and the other two fibres as elastic with the high elastic modulus 5.7E is expected to give a good approximation.

Cylindrical coordinates are used for the numerical analysis of the axisymmetric cell. The displacement components on the base vectors of the cylindrical reference coordinate system are denoted u^i, and the Lagrangian strain tensor is given by

$$\eta_{ij} = \tfrac{1}{2}(u_{i,j} + u_{j,i} + u^k_{,i}u_{k,j}) \tag{2.7}$$

where $(\ )_{,i}$ denotes the covariant derivative in the reference frame. The principle of virtual work takes the form

$$\int_V \tau^{ij}\delta\eta_{ij}\,\mathrm{d}V + \int_{S_I} (T_n\delta u_n + T_t\delta u_t)\,\mathrm{d}S = \int_S T^i\delta u_i\,\mathrm{d}S \tag{2.8}$$

where V and S denote the reference volume and surface of the cell analysed, S_I denotes the internal surface, at which debonding may take place, and T^i are the specified nominal surface tractions. The normal displacement difference u_n and the tangential displacement difference u_t across the interface are expressed in terms of the axial displacement of the rigid fibre and the displacements u^i on the matrix side of the interface.

Approximate solutions of (2.8) are obtained by a linear incremental method, using a finite element approximation of the displacement fields. The elements used are quadrilaterals, each built up of four triangular axisymmetric linear displacement elements, as in previous analyses of fibre debonding (Tvergaard, 1990b, 1991).

A special Rayleigh–Ritz finite element method (Tvergaard, 1990b, 1976) is used to implement the boundary conditions representing the transversely staggered fibres, to control the numerical stability during debonding, and to enforce a fixed ratio, $\rho = \sigma_2/\sigma_1$, of the average true stresses in the transverse and axial directions, respectively.

3. Results

In the present computations the material parameters are chosen to represent the particular aluminium alloy 2124-SiC whisker-reinforced composite investigated by Christman et al. (1989), that has also been modelled in the fibre debonding study of Tvergaard (1990b). For this material Tvergaard (1990a) has found that the uniaxial stress–strain curve of the matrix is reasonably well approximated by the power law (2.3)

with $\sigma_y/E = 0.005$ and $n = 7.66$ (i.e. $\sigma_y = 0.3$ GPa and $E = 60$ GPa), and the value of Poisson's ratio is taken to be $v = 0.3$.

Three different material geometries are considered here, as illustrated by the initial, undeformed meshes in Fig. 3. All three material geometries have $\ell_f/r_f = 5$ and $r_f/r_c = 0.538$, and the same total fibre volume fraction $f = 0.13$. In addition, material A has only one type of fibre, with $\ell_f/\ell_c = 0.448$, just like materials analysed previously (Tvergaard, 1990a,b). Material B is specified by $\ell_f/\ell_c = 0.224$, $r_1 = r_2 = r_f$, $\ell_1/\ell_c = 0.112$, $\ell_2/\ell_c = 0.112$, $a_1/\ell_c = 0.448$ and $a_2/\ell_c = 0.785$. Material C is rather similar to material A, but here $\ell_1/\ell_c = 0.149$, $\ell_2/\ell_c = 0.075$, $a_1/\ell_c = 0.500$ and $a_2/\ell_c = 0.925$. Thus, in material C ℓ_2 is the half-length of a fibre that continues across the symmetry plane at $x^1 = \ell_c$, similar to the fibre subject to debonding, where ℓ_f is the half-length of a fibre continuing across the symmetry plane at $x^1 = 0$.

Fig. 4 shows computed stress–strain curves for the three different materials subject to overall uniaxial tension ($\rho = \sigma_2/\sigma_1 = 0$). The strength of the fibre–matrix interface is here modeled by using the parameter values $\sigma_{max}/\sigma_y = 5$, $\delta_n = \delta_t = 0.02r_f$ and $\alpha = 1$ in (2.4)–(2.6). In all cases debonding initiates at the sharp fibre edge, where high concentrations of stress and strain develop, and subsequently debonding develops over the end surface of the long fibre while the overall stress decays rapidly, as is seen in Fig. 4 for all three curves at a strain around $\epsilon_1 \simeq 0.025$. After this point the three curves are rather close to each others, while tangential debonding and fibre pull-out occurs along the sides of the longer fibres. Prior to any debonding, i.e. prior to the stress peaks, material A shows significantly higher stiffness and stress carrying capacity than the other two materials. This is not surprising, as all fibres in material A have the high aspect ratio 5, and it is known from earlier studies (Tvergaard, 1990a) that the material response in the absense of debonding is very sensitive to the fibre aspect ratio, for a given volume fraction of fibres. During the initial debonding process the reduction of the stress level is much larger for material A than for the other two materials, which is related to the fact that in material A all fibres debond simultaneously, while in the other two materials some of the fibres remain fully bonded. After debonding at the fibre end, during the process of fibre pull-out, material C shows a slightly higher stress level than the other two materials. This is not surprising either, since both materials B and C have some fibres that remain fully bonded, but in material C these fibres have an aspect ratio 33% higher than those in material B, for the same fibre volume fraction, and therefore, based on the results in Tvergaard (1990a) a higher stress carrying capacity would be expected.

Fig. 5 shows the deformed meshes corresponding to the end stages of the three computations in Fig. 4, where the long fibre has debonded at the end and along part of the cylindrical side near the end. The cylindrical sides of the unit cells are noticeably deformed in Fig. 5, and it is seen that an outward wave at
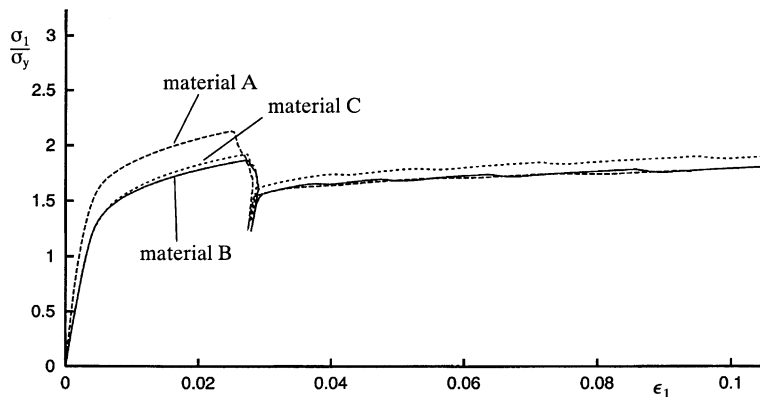

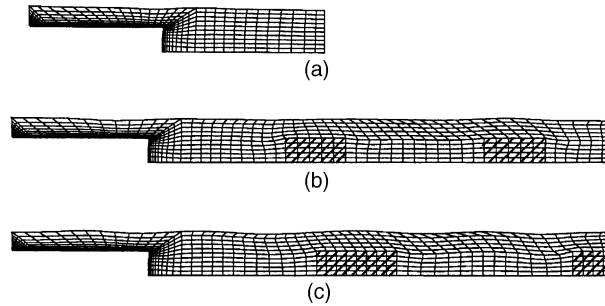Fig. 4. Stress–strain curves predicted for $\rho = 0$, $n = 7.66$ and $\sigma_{max}/\sigma_y = 5$.

Fig. 5. Deformed meshes for $\rho = 0$, $n = 7.66$ and $\sigma_{max}/\sigma_y = 5$: (a) material A at $\epsilon_1 = 0.094$; (b) material B at $\epsilon_1 = 0.111$ and (c) material C at $\epsilon_1 = 0.111$.

one end of the cell side fits into an inward wave at the other end of the cell side, as is needed to follow the identical neighbouring cell rotated 180° so that it points in the opposite directions (see Fig. 1(a) and Tvergaard (1990b)). No deformation is visible for the shorter fibres in Figs. 5(b) and (c), which are shown hatched.

In spite of the result in Tvergaard (1990a) that predictions for elastic or rigid fibres differ rather little, it is noted that prior to debonding the most stiff response in Fig. 4 is that for material A where all fibres are approximated as rigid, since all fibres in material A undergo debonding. To check this further, the curve for material B in Fig. 4 has been recomputed with the elastic fibres ten times as stiff, such that $E_f/E = 57.0$. The comparison in Fig. 6 confirms that the fibre elastic modulus $E_f = 5.7E$ is high enough, so that a good approximation is obtained by representing the debonding fibre as rigid, while the short perfectly bonded fibres are elastic.

The curves in Fig. 7 are obtained for the same loading conditions and material parameters as those considered in Fig. 4, except that the interface strength is halved, so that $\sigma_{max}/\sigma_y = 2.5$. This gives much earlier debonding at the fibre ends. Also, it is seen in Fig. 7 that the strain for the onset of debonding in material A is significantly smaller than the corresponding strain for the other two materials, which was not found in Fig. 4. After debonding at the fibre end the curve for material C stays above the other two, as in Fig. 4. This is still related to the fact that fibres remaining bonded in material C have larger aspect ratio than those in material B.
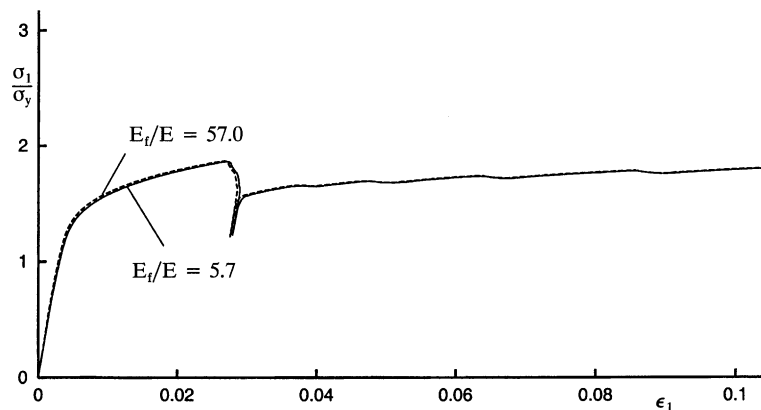

Fig. 6. Comparision of predictions for the fibre elastic modulus $E_f = 5.7E$ with a 10 times higher elastic modulus of the fibres. Stress–strain curves for material B (Fig. 3(b)), with $\rho = 0$, $n = 7.66$ and $\sigma_{max}/\sigma_y = 5$.
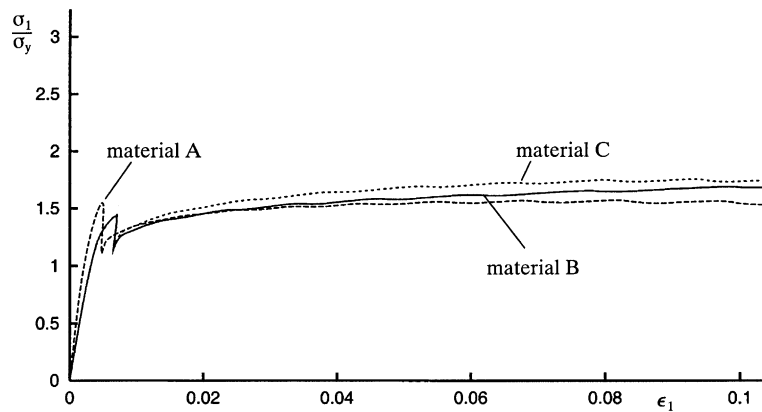
Fig. 7. Stress–strain curves predicted for $\rho = 0$, $n = 7.66$ and $\sigma_{max}/\sigma_y = 2.5$.

In the case of Fig. 8 all material parameters are identical to those considered in Fig. 4, but here the stress triaxiality is increased by taking $\rho = \sigma_2/\sigma_1 = 0.5$. This results in significantly higher stress levels before plastic flow develops in the matrix material, and therefore the onset of failure by debonding at the ends of the longer fibres takes place at much smaller overall strains than those predicted in Fig. 4. Here, the onset of debonding occurs at a significantly smaller strain in material A than in the other two materials, as was also found in Fig. 7, and after debonding the curve for material C is above the other two curves, as in Figs. 4 and 7. However, at a strain about 0.058 the curve for material C drops far below that for material B. This is a result of necking between neighbouring voids growing around fibres that have debonded from the matrix, as is better understood by considering the deformed unit cells in Fig. 9, showing also the contours of maximum principal logarithmic strain.

After debonding at the fibre end and along part of the fibre side Fig. 9 shows that the voids around debonded fibres tend to expand in the radial direction, due to the increased stress triaxiality. Now, for the
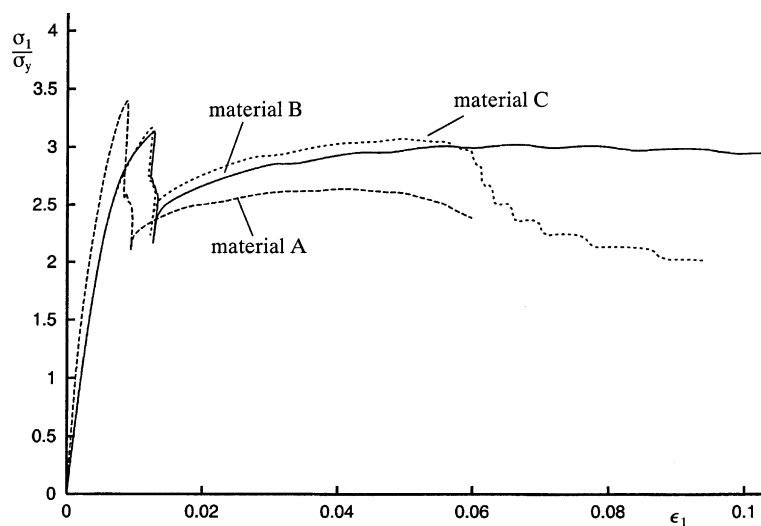

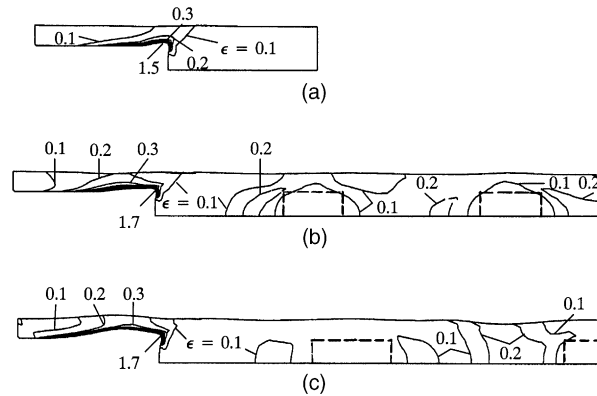Fig. 8. Stress–strain curves predicted for $\rho = 0.5$, $n = 7.66$ and $\sigma_{max}/\sigma_y = 5$.

Fig. 9. Contours of maximum principal logarithmic strain for $\rho = 0.5$, $n = 7.66$ and $\sigma_{max}/\sigma_y = 5$: (a) material A at $\epsilon_1 = 0.060$; (b) material B at $\epsilon_1 = 0.108$ and (c) material C at $\epsilon_1 = 0.094$.

periodic pattern of fibres considered here, the neighbouring cell is rotated 180° relative to the cell in Fig. 9, as illustrated in Figs. 1(a) and 2, and the following neighbour is oriented as the cell analysed. Therefore, the voids around debonded fibres in Figs. 9(b) and (c) would like to interact with the identical voids two cells away in the radial direction. This is prevented in Fig. 9(b) by the elastic particle between the two voids, while in Fig. 9(c) there is only matrix material between the adjacent voids, and therefore a neck develops, leading to the rapid load drop for material C in Fig. 8. The void around the fibre end in Fig. 9(a) interacts with that in the neighbouring cell, as has also been found in previous analyses for a cell containing only one type of fibre (Tvergaard, 1993, 1995), and this also gives some load drop at the end of the curve for material A in Fig. 8.

The effect of strain hardening is studied in Figs. 10 and 11. As in Fig. 4 the composite is subjected to overall uniaxial tension ($\rho = 0$), but in Fig. 10 the matrix material is more high hardening, with $n = 4$, while the matrix material in Fig. 11 has lower hardening, $n = 12$. With high hardening the stress level in the material increases more rapidly, and therefore debonding initiates at a smaller overall strain. Therefore, compared to Fig. 4, the onset of debonding occurs at a smaller strain in Fig. 10 and at a larger strain in
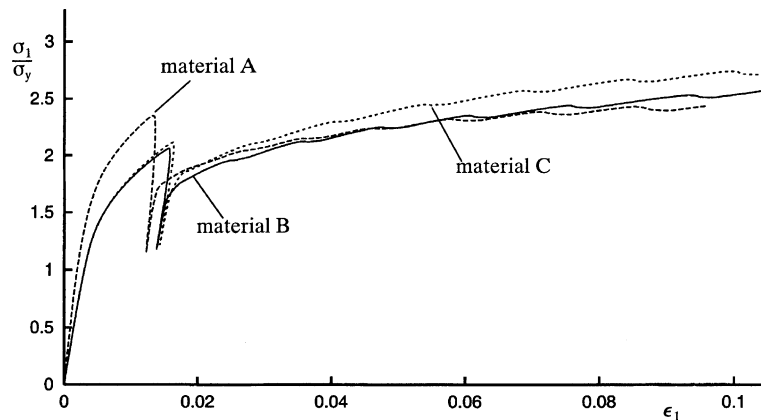

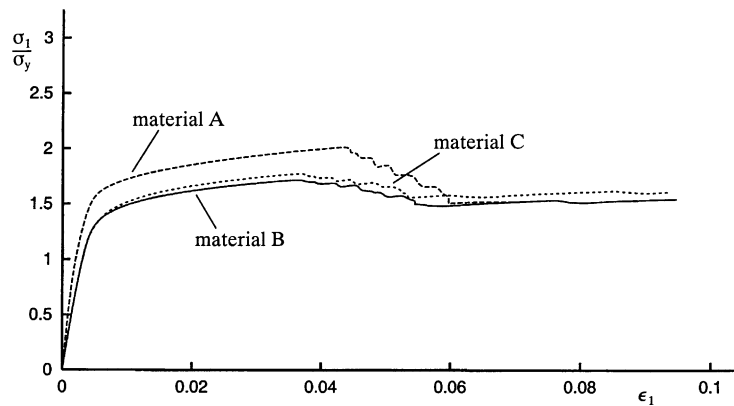Fig. 10. Stress–strain curves predicted for $\rho = 0$, $n = 4$ and $\sigma_{max}/\sigma_y = 5$.

Fig. 11. Stress–strain curves predicted for $\rho = 0$, $n = 12$ and $\sigma_{max}/\sigma_y = 5$.

Fig. 11. In both figures material A shows the highest stress level prior to debonding and material C shows the highest stress level after debonding, as was also discussed in relation to Figs. 4 and 7.

4. Discussion

For metals reinforced by short brittle fibres most analyses of damage evolution have been based on studies for a characteristic volume containing just a single fibre, which represents a simple periodic array of fibres. Effects of non-uniform fibre distributions, including fibre clustering, are important in practice, but in general studies of such effects would require full three dimensional analyses of large unit cells, containing several fibres of different shape and spacings. Analyses of cell models containing several non-uniformly distributed fibres are quite feasible with the assumption of plane strain conditions, but plane strain models have the disadvantage that the fibre geometry is not at all realistically represented. Three dimensional studies for metal matrix composites have been carried out, but there are only few studies accounting for full damage evolution, as e.g. the studies of Tvergaard (1998, 2001), considering ductile matrix failure, since the description of final failure with the full evolution of open cracks around fibres tends to increase the computing time by a large factor.

The present extension of a special axisymmetric cell-model to include a number of differently shaped fibres within each cell has made it possible to study some effects of non-uniform fibre distributions, while still retaining realistic fibre geometries, and avoiding the large computing times associated with full damage evolution and crack formation in three-dimensional analyses. One such effect is shielding of a debonding fibre by neighbouring fibres that do not debond. Some of the analyses here have shown a significant shielding effect (Figs. 7, 8 and 10), in that the onset of debonding occurs at a larger strain when the debonding fibre is surrounded by fibres that do not debond. However, the effect is less clear in Figs. 4 and 11, where the onset of debonding occurs at a larger plastic strain level. Here, in spite of the shielding in materials B and C, the plastic redistribution of the stress fields may have resulted in the longest fibre carrying a relatively higher part of the load, thus promoting debonding of the long fibre. In conclusion, shielding can delay the onset of debonding, but there is competition with other mechanisms that can have an opposite effect.

After debonding at the fibre end, during the stage of gradual fibre pull-out, it is found that the average stress level is determined by the aspect ratio of the fibres that are still bonded to the matrix. Therefore, material C shows higher stress carrying capacity after debonding. However, also in this range there can be a

shielding effect, as is illustrated in Fig. 8 for a material under transverse tension, so that the high stress triaxiality gives rise to void growth in the transverse direction. Here, shielding from the neighbouring bonded fibres prevents such void growth in material B, but not in material C due to different locations of the neighbouring bonded fibres.

It will be of interest, in subsequent studies, to consider other fibre distributions than those analysed here. Also fibre fracture is an important failure mechanism in metal matrix composites, and further studies can show whether the interaction between the two failure mechanisms would be affected by the distribution of fibres of different size.

References

Christman, T., Needleman, A., Suresh, S., 1989. An experimental and numerical study of deformation in metal–ceramic composites. Acta. Metall. 37, 3029–3050.

Divecha, A.P., Fishman, S.G., Karmarker, S.D., 1981. Silicon carbide reinforced aluminum-a formable composite. J. Met. 33, 12–17.

Dvorak, G.J., Zarzour, J., Benveniste, Y., 1992. Fracture of fibrous metal matrix composites-IV. Plastic zones, local stresses and fracture strength. Eng. Fract. Mech. 42, 501–517.

Finot, M., Shen, Y.-L., Needleman, A., Suresh, S., 1994. Micromechanical modelling of reinforcement fracture in particulate-reinforced metal–matrix composites. Metall. Mater. Trans. 25A, 2403.

McDanels, D.L., 1985. Analysis of stress–strain, fracture, and ductility behaviour of aluminum matric composites containing discontinuous silicon carbide reinforcement. Metall. Trans. A 16, 1105–1115.

Needleman, A., 1987. A continuum model for void nucleation by inclusion debonding. J. Appl. Mech. 54, 525–531.

Needleman, A., Nutt, S.R., Suresh, S., Tvergaard, V., 1993. Matrix, reinforcement and interfacial failure. In: Suresh, S., Mortensen, A., Needleman, A. (Eds.), Fundamentals of Metal Matrix Composites. Butterworth-Heinemann, Boston, MA, pp. 233–250.

Nutt, S.R., Needleman, A., 1987. Void nucleation at fibre ends in Al–Sic composites. Scr. Metall. 21, 705–710.

Tvergaard, V., 1976. Effect of thickness inhomogeneities in internally pressurized elastic–plastic spherical shells. J. Mech. Phys. Solids 24, 291–304.

Tvergaard, V., 1990a. Analysis of tensile properties for a whisker-reinforced metal–matrix composite. Acta. Metall. Mater. 38, 185–194.

Tvergaard, V., 1990b. Effect of fibre debonding in a whisker-reinforced metal. Mater. Sci. Eng. A 125, 203–213.

Tvergaard, V., 1991. Micromechanical modelling of fibre debonding in a metal reinforced by short fibres. In: Dvorak, G. (Ed.), Inelastic Deformation of Composite Materials. Springer, Berlin, pp. 99–111.

Tvergaard, V., 1993. Model studies of fibre breakage and debonding in a metal reinforced by short fibres. J. Mech. Phys. Solids 41, 1309–1326.

Tvergaard, V., 1995. Fibre debonding and breakage in a whisker-reinforced metal. Mater. Sci. Eng. A 190, 215–222.

Tvergaard, V., 1998. Effects of ductile matrix failure in three dimensional analysis of metal matrix composites. Acta. Mater. 46, 3637–3648.

Tvergaard, V., 2001. Three-dimensional analysis of ductile failure in metal reinforced by staggered fibres. Model. Simul. Mater. Sci. Eng. 9, 143–155.

Zok, F., Embury, J.D., Ashby, M.F., Richmond, O., 1988. The influence of pressure on damage evolution and fracture in metal–matrix composites. In: Andersen, S.I. et al. (Eds.), Mechanical and Physical Behaviour of Metallic and Ceramic Composites. Risø National Laboratory, Denmark, pp. 517–526.